

ENGINEERING

Dynamic drives allow independent control of material bits for targeted memory

Eduardo Gutierrez-Prieto^{1†}, Colin M. Meulblok^{2,3†}, Martin van Hecke^{1,3*}, Pedro M. Reis¹

Mechanical metamaterials with bistable elements can store vast amounts of information, but writing these memories requires impractical local control or lengthy multicycle protocols. We overcome this limitation with a dynamic control strategy that accesses any configuration in a single global drive cycle by leveraging the system's sensitivity to the drive and its time derivatives. We realize this strategy with bistable beams on a rotating platform, where drive cycles become orbits in a control space of angular velocity and acceleration. State changes occur when these orbits cross switching thresholds, which we rationally design so that each state can be accessed by a single drive orbit. We construct a five-bit system and demonstrate its full addressability by selecting drive orbits that write all 26 uppercase letters of the alphabet in ASCII representation. This dynamic control paradigm offers a general route toward smart, remotely operated devices across various physical domains.

INTRODUCTION

Mechanical structures made from bistable elements can store configurational memories (1–12) to enable tunable stiffness (13–15), sequential shape-morphing (16–18), and computation (1–3, 19–24). While control over configurations is essential, it typically requires local and individual access to all elements (13–15). Here, we introduce a dynamic control strategy that enables transitions between any pair of configurations within a single global drive cycle by exploiting sensitivity to different (orders of) derivatives of the driving. We illustrate this approach using bistable beams that snap through based on their collective rotation rate and acceleration. Through rational design and selection of drive cycles, we demonstrate targeted transitions along controllable pathways, including the writing of five-bit memories that encode all alphabetic characters. This form of dynamical control can be generalized to inertial, fluidic, electromagnetic, and electronic systems, thus providing a powerful method for writing memories and enabling smart, remotely controllable devices for applications in microfluidics, implants, smart infrastructure, and underwater or medical robotics.

Developing driving protocols that access all configurations of mechanical systems of material bits (mbits), comprising bistable elements, is essential for the functionality of multistable (meta)materials (1–24). Unfortunately, individually controlling each mbit becomes impractical as their number N grows large (13–15), and although it is possible to design mbits such that a single global driving field can access all states, such strategies require baroque driving protocols featuring up to N drive cycles (4, 25). However, there are several examples of physical systems that also respond to the driving rate: In mechanics, driving forces depend on the configuration and motion (inertia); in fluids, on static pressure and flow (viscosity); and in electronics, currents depend on voltage (resistance) and its rate of change (capacitance). This poses the question of how and whether dynamic control strategies can be developed that allow access to all 2^N states using a single global drive cycle.

¹Flexible Structures Laboratory, Institute of Mechanical Engineering, École Polytechnique Fédérale de Lausanne (EPFL), Lausanne, Switzerland. ²Huygens-Kamerlingh Onnes Lab, Universiteit Leiden, Leiden, Netherlands. ³AMOLF, Amsterdam, Netherlands.

*Corresponding author. Email: mvhecke@gmail.com

†These authors contributed equally to this work.

To address this challenge, we introduce a rational design principle to select dynamic driving protocols that together enable a global driving signal to steer transitions between arbitrary mbit states along selectable pathways. As we show, at the core of our strategy lies the fact that dynamic driving can be naturally represented as driving orbits in a multidimensional space, where the different axes represent the relevant derivatives of the drive. The ability to connect regions in this space to different stable configurations—unconstrained by the well-ordering of one-dimensional space that governs quasistatic driving—is crucial for enabling any-to-any transitions and simplifies both system design and driving cycle selection.

RESULTS

While the strategy introduced above should be general for a wide range of physical systems, we focus on a mechanical implementation where each mbit i is a prebuckled, double-clamped elastic beam mounted on a rotating disk, with its buckling direction defining the binary state s_i (Fig. 1A; see the Supplementary Materials and movie S1) (3, 26, 27). The angular velocity $\Omega(t)$ and time-derivative $\dot{\Omega}(t)$ control the radial centrifugal forces $f_\Omega \sim \Omega^2$ and azimuthal Euler forces $f_E \sim \dot{\Omega}$ that jointly control the switching of the mbits (Fig. 1B) (28). This interplay enables $\Omega(t)$ to serve as a dynamic control input for selectable transition pathways.

We demonstrate this selectivity with system I (Fig. 1 and movie S2), which comprises two mbits that differ in compressive strain ϵ and tilt angle θ (see “System parameters” and the Supplementary Materials). We consider the transition pathways under two dynamic (harmonic) driving protocols $\Omega(t) = -a_j \sin(2\pi f_j t)$, where a_j is fixed and f_j is varied, to induce transitions between collective states $S = (s_1 s_2) = (00)$ and (11) . Notably, while for f_1 the system goes through intermediate state (10) , for f_2 , the pathway from (00) to (11) exhibits a different intermediate state (01) (Fig. 1, E and H, and movie S2). To understand how dynamic driving shapes transition pathways, we map driving protocols to orbits in the $\Omega - \dot{\Omega}$ plane (Fig. 2A and movie S2). Each protocol traces a distinct elliptical orbit, along which we plot the observed states and the up ($s_i: 0 \rightarrow 1$) and down ($s_i: 1 \rightarrow 0$) transitions of both mbits, revealing that switching thresholds depend on both Ω and $\dot{\Omega}$ (Figs. 1, C to H, and 2A). A central insight is that transitions occur along up curves u_i ($s_i: 0 \rightarrow 1$) and

Copyright © 2026 The Authors, some rights reserved; exclusive licensee American Association for the Advancement of Science. No claim to original U.S. Government Works. Distributed under a Creative Commons Attribution NonCommercial License 4.0 (CC BY-NC).

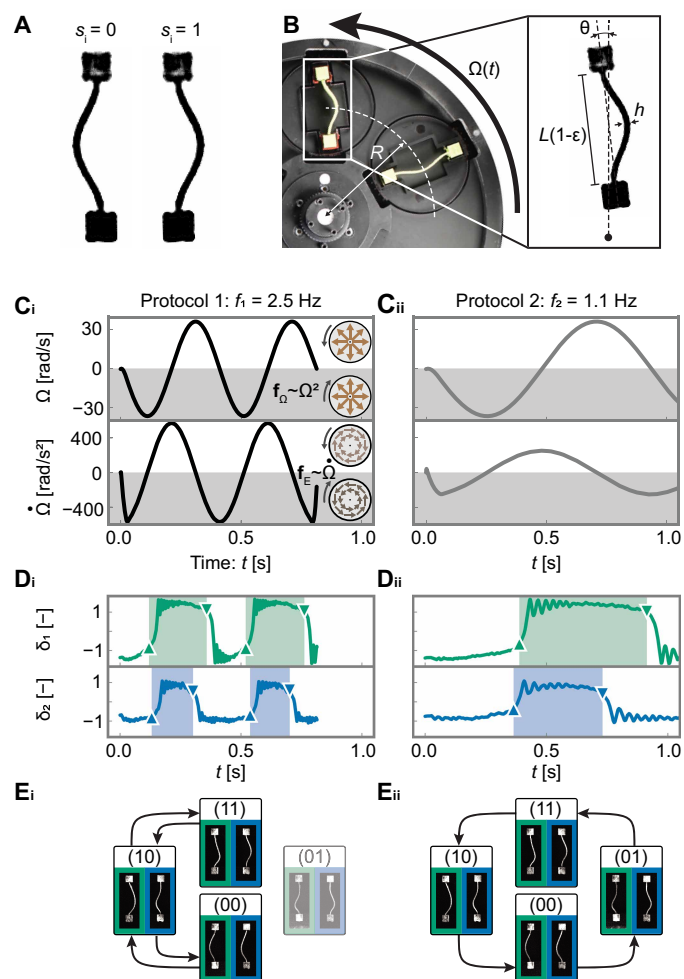


Fig. 1. Dynamic driving of mbits. (A) Buckled beams form mbits whose buckling direction defines their state: $s_i = 0$ for counterclockwise and $s_i = 1$ for clockwise deflection. (B) Rotating disk apparatus showing system I and design parameters (see the Supplementary Materials). (C) Driving protocols $\Omega(t) = -a_i \sin(2\pi f_i t)$, where $a_1 = a_2 = 36.5$ rad/s and frequencies f_i as indicated. (D) Evolution of beam midspan δ_i showing distinct switching sequences connecting $S: (00) \rightarrow (11)$ via either (01) or (10). (E) Corresponding pathways of states.

down curves d_i ($s_i: 1 \rightarrow 0$) in the $\Omega - \dot{\Omega}$ plane, which can be identified by aggregating data from many elliptical driving orbits (Fig. 2A; see the Supplementary Materials). The up and down transition curves for each element partition the plane into domains corresponding to distinct stable states. Note that all states are stable at the origin (i.e., without driving) and that only crossings oriented away from the origin can produce transitions (Fig. 2A). Intersections of transition curves are key; for example, the two elliptical driving orbits cross u_1 and u_2 on opposite sides of their intersection, thus producing the distinct pathways: $(00) \rightarrow (10) \rightarrow (11)$ and $(00) \rightarrow (01) \rightarrow (11)$ (Fig. 2A and movie S2).

We leverage the principles elucidated above to selected driving orbits for system I so that any of its four binary states can be written (Fig. 2, B to E, and movie S3). We focus on orbits that start and end at the origin, where all states are stable. Note that any orbit with appropriate orientation (Fig. 2A) can be mapped to a physically realizable input function $\Omega(t)$ (see the Supplementary Materials). Reaching a

target state requires changing mbits from $0 \rightarrow 1$ or $1 \rightarrow 0$, which demands appropriate crossings of the corresponding u_i and d_i curves. For example, an orbit that crosses only d_1 and d_2 zeroes both mbits and produces $S = (00)$, regardless of the initial state (Fig. 2B). Note that specific switching curve topologies complicate orbit selection. Naively, one might expect that the target state $S = (01)$ can be written by simply crossing d_1 and u_2 , but any such orbit also crosses d_2 (Fig. 2C). In system I, writing the target state $S = (01)$ requires an orbit that crosses d_2, d_1 , and then u_2 (Fig. 2C). Similarly, all other target states of system I can be reached by selecting appropriate orbits (Fig. 2, D and E). These examples demonstrate that dynamic control enables the rational selection of targeted orbits capable of writing any combination of mbits in system I, robust to external vibrations and the manufacturing tolerances of laser-cut fabrication.

To be able to write any possible state in a system with an arbitrary number of mbits, we first introduce hierarchically organized switching curves as a design target and then show how the physical mbits can be designed to realize such curves. As a schematic example, consider three up curves that intersect such that there is a range in driving space where each is closest to the origin (Fig. 3A). Initializing the system in state (000), it is then possible to select driving orbits $O(s_i)$ that set mbit i to 1 (Fig. 3A). Setting multiple mbits to 1 can be achieved by chaining such orbits or by selecting more complex multicrossing driving orbits such as $O(s_3, s_1)$; this freedom allows control of intermediate states (Fig. 3A). Our proposed hierarchical design can be generalized to encompass more mbits and is the prime design target to realize systems with highly targeted switching behavior, as we demonstrate next.

We explore the real-space design of the mbits by investigating the dependence of the switching curve on the tilt angle θ_i and the compressive strain ϵ_i of the corresponding mbits. To guide us with a rational design, we use a von Mises-truss model comprising a mass connected to two linear springs (see the Supplementary Materials). This model system captures the bistability of the mbits and, when subjected to centrifugal and Euler forces, allows to study the properties of the switching curves as a function of θ_i and ϵ_i (Fig. 3B) (29–31). We first fix $\theta = 0$ and find that the switching curves can be moved away from the origin by increasing ϵ , which controls the energy barrier between the $s = 0$ and $s = 1$ states (Fig. 3C_i). Second, nonzero tilt angles ($\theta \neq 0$) break the symmetry between the up and down switching curves, allowing widening of the u curves and narrowing of the d curves by increasing θ (Fig. 3C_{ii}). Systematically varying the design parameters (θ_i and ϵ_i) enables the construction of the hierarchical switching curves: Up-curves require increasing strain and tilt, while down-curves combine increasing strain with decreasing tilt (Fig. 3D). Hence, geometric control of the mbits facilitates designing systems with targeted hierarchical switching curves.

Last, we design a five-mbits system, whose collective state can be written with a single clockwise driving orbit starting and terminating at $(\Omega, \dot{\Omega}) = (0, 0)$. As a first step, we design the switching curves such that a target state $(t_1 t_2 t_3 t_4 t_5)$ can be reached from an initial arbitrary state (xxxxx). Hierarchical design of either all up or all down switching curves is sufficient to do so in principle, but, instead, to enhance robustness, it is advantageous to leverage hierarchical ordering of subsets of the up and down curves, so that less critical intersections are required. Here, we opt for a design where (u_1, u_2) and (d_3, d_4, d_5) are hierarchically ordered, but note that other hierarchical orderings are valid too. We then use orbits that consist of a first erase phase, where the state evolves to (00111) via the intermediate

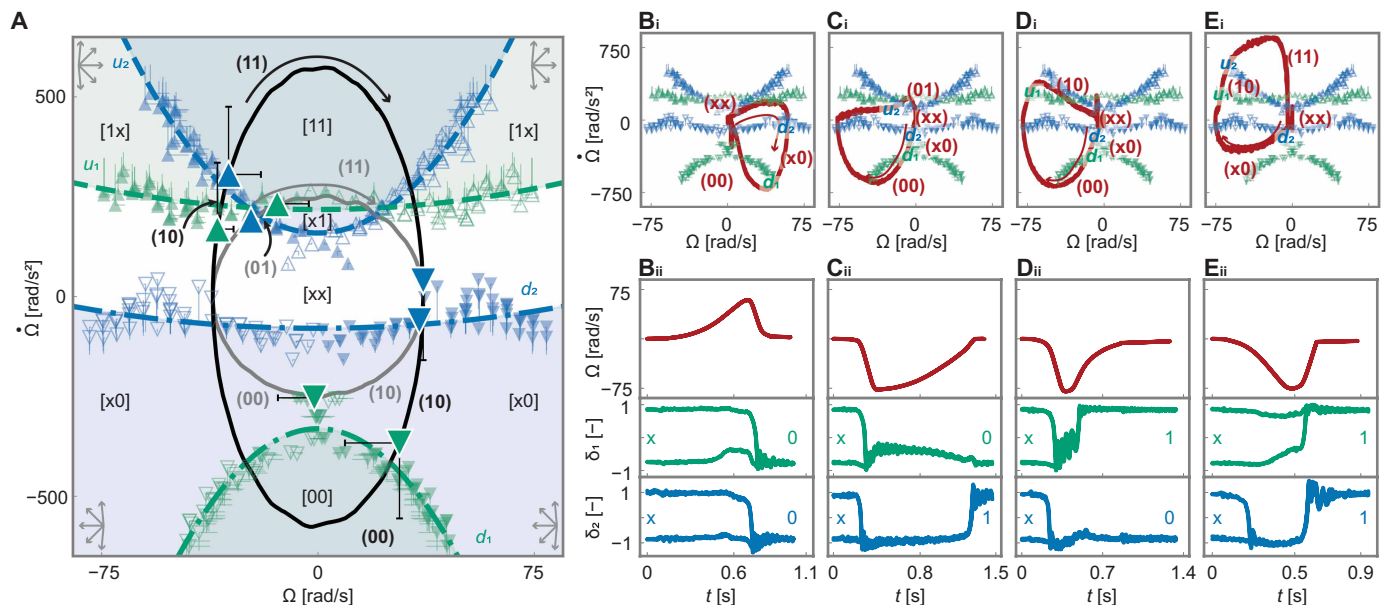


Fig. 2. Orbits, transitions, and states. (A) Data for system I in the $(\Omega, \dot{\Omega})$ -plane, where green and blue correspond to mbits one and two, respectively. The ellipses correspond to protocol 1 (black) and 2 (gray), with arrows indicating the required clockwise orientation. The observed up transitions (Δ), down transitions (Δ), and states highlight the difference in intermediate states (bold). The switching onset for harmonic protocols with (frequency $f_j = 1.5$ Hz, drive amplitude $a_j \in [5.0, 80.0]$ rad/s) are shown as faint symbols with associated uncertainties (see the Supplementary Materials). The dashed and dot-dashed lines are quadratic fits serving as guides to the eye for the up- and down-switching curves, respectively (see the Supplementary Materials). These lead to partitions (shaded regions) where one or more collective states (square brackets) are stable, where “x” indicates mbits that can be both 0 and 1. The arrows indicate the allowed orbit directions in each quadrant (open intervals of size π). [(Bi) to (Ei)] Selected orbits that write specific targeted states: (B) (00), (C) (01), (D) (10), and (E) (11). [(Bii) to (Eii)] Angular velocity $\Omega(t)$ corresponding to selected orbits (top) and corresponding evolution of the midspan displacement of beams one (middle) and two (bottom), starting from any of four initial states, demonstrating how the final state is independent of the initial configuration.

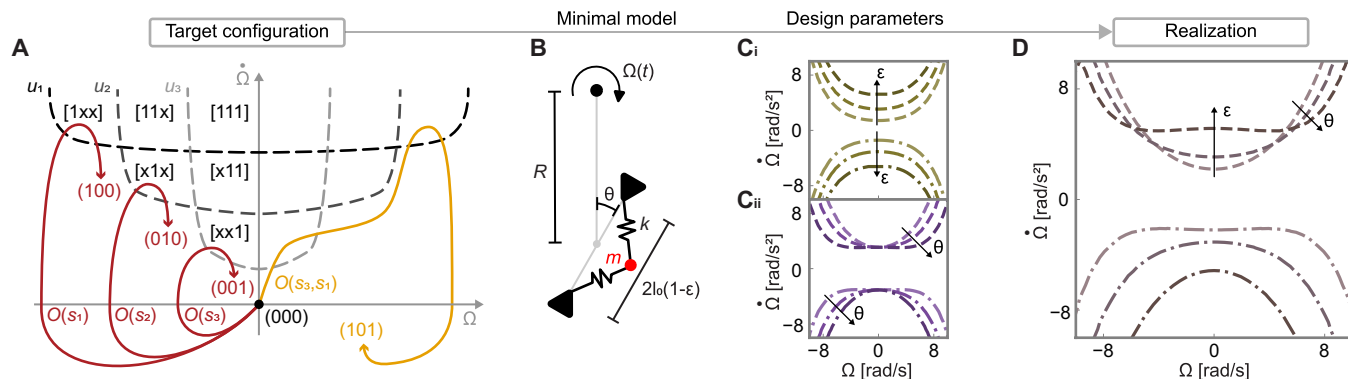


Fig. 3. System design. (A) Schematic set of hierarchical switching curves (u_1, u_2, u_3) with selected orbits that enable the writing of arbitrary states: starting from state (000), the orbits $O(s_1), O(s_2), O(s_3)$, and $O(s_3, s_1)$ write states (100), (010), (001) and (101). (B) Minimal model for mbits, comprising two linear springs (spring constant k and rest length l_0), each connected to a central mass m ; the key design parameters are the compressive strain ϵ and tilt angle θ . (C) Representative trends for the transition curves obtained from the minimal model with parameters ϵ and θ (arrows). Top: $\epsilon = (0.03, 0.05, 0.07)$ with $\theta = 0$. Bottom: $\theta = (-3^\circ, 0^\circ, 3^\circ)$ with $\epsilon = 0.05$. Experimental curves show similar trends (see fig. S3). (D) Hierarchical up transition curves for $(\epsilon, \theta) = [(0.04, -3^\circ), (0.05, 0^\circ), (0.07, 4^\circ)]$.

state (11111), and then a write phase, where the first two bits can be switched $0 \rightarrow 1$ and the last three bits can be switched $1 \rightarrow 0$ (Fig. 4A). In such a scenario, the precise locations of the nonhierarchical curves are less critical, provided that (u_1, u_2) can be crossed without crossing (u_3, u_4, u_5) , and (d_1, d_2) are crossed before crossing (d_3, d_4, d_5) , so that in the erase phase, we can reach state (00111) (Fig. 4A). Using our numerical toolbox and some experimental fine-tuning, we realize the

target ordering of the switching curves experimentally in system II (Fig. 4B; see the Supplementary Materials).

To demonstrate the expressive capabilities of our approach, we construct a library of driving orbits capable of writing all 26 binary states S that encode the Latin uppercase characters of the alphabet (see fig. S4). Selecting appropriate orbits, as an example, we sequentially drive our five-mbit system to write the word “ORBIT” (Fig. 4,

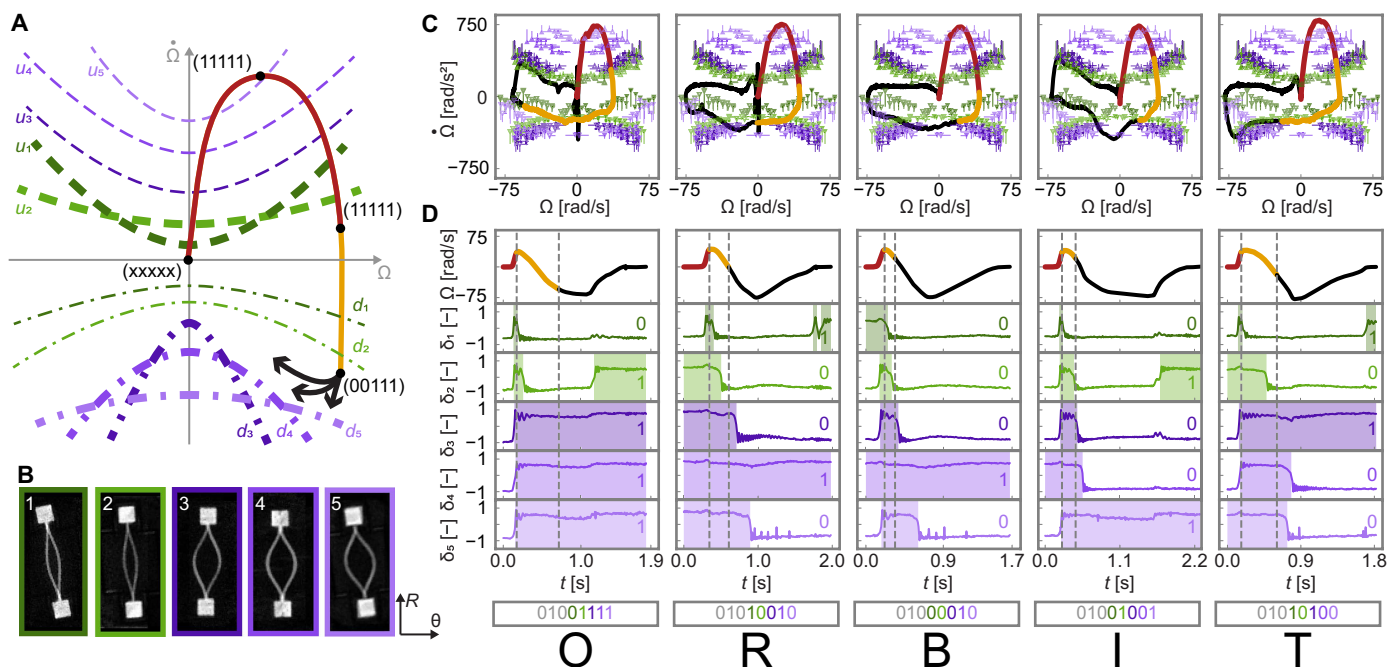


Fig. 4. Writing arbitrary states in system II. (A) Target hierarchical organization of the curves (u_1, u_2) and (d_3, d_4, d_5) (bold), together with appropriate placement of the other switching curves. Starting out from arbitrary state (xxxxx), the first phase of the erase orbit (red) sets all bits, reaching state (11111), whereas the second phase (gold) resets the first two bits reaching state (00111), after which the writing phase commences (black). (B) System II is composed of five mbits with rationally designed tilt angle and compression that lead to the targeted ordering of switching curves. (C) Driving orbits corresponding to specific characters (red: erase phase one, gold: erase phase two, black: writing phase). (D) Experimental driving protocol and beam evolution demonstrate how dynamic control enables writing ORBIT (see movie S4). The ASCII encoding standard is used to map the bit strings to the Latin characters (46). Although ASCII requires eight bits, the first three bits are identical for all uppercase characters; hence, we write the remaining five bits. Below each orbit, the full bit string is shown, with colors labeling the mbits and gray indicating the three shared bits.

C and D; see the Supplementary Materials and movie S4). This capability of writing arbitrary words using Latin characters highlights that dynamic control of a rationally designed mbit system offers a powerful strategy to write and erase information.

DISCUSSION

We stress that dynamic driving extends beyond rotation, encompassing inertial or viscous effects in mechanics (32–36), and, more broadly, dynamic effects in fluid flow (37, 38), chemical reactions (39), and electronic circuits (40). For instance, mbits could function as bistable valves to enable global reconfiguration of centrifugal microfluidic circuits (41). Similarly, electronic implementations of mbits can easily be made time dependent using standard RC circuits, where voltage and its time derivative (analogous to Ω and $\dot{\Omega}$) allow a global time-dependent signal to control several mbits independently. Last, in soft robotics, bistable elements with distinct intrinsic timescales could be differentially triggered by varying the rate of pneumatic or hydraulic actuation, enabling gait control that adapts to ambient viscosity (36).

The systematic exploration of diverse dynamically driven mbit platforms will enable agile information encoding for future smart and multifunctional devices. Although the current implementation is not optimized for energy efficiency, dynamic global driving is compatible with energy-efficient bit switching via appropriate material and design choices. Furthermore, the use of high-precision micro- or nanoelectromechanical systems (MEMS or NEMS) fabrication methods could reduce geometric tolerances by orders of magnitude, while metallic

materials in optimized geometries could reduce snapping timescales to microseconds, both significantly tightening threshold uncertainty. Energy dissipation per switching event is minimal and does not accumulate across elements due to sequential switching along the orbit. When combined with hybrid (global and local) driving strategies, in which multiple groups of mbits are dynamically driven independently, our approach provides a rational and scalable pathway toward much larger arrays.

MATERIALS AND METHODS

Experimental methodology

Beams

The beams are fabricated by casting a silicone-based elastomer [VPS32, Zhermack Elite Double 32, with Young's modulus $E = 1.22 \pm 0.05$ MPa, Poisson's ratio $\nu \approx 0.5$, and density $\rho = (1.17 \pm 0.01) \cdot 10^3$ kg m⁻³] (42, 43), using a fully enclosed mold. VPS32 exhibits a highly elastic mechanical response with minimal viscoelasticity, rate dependence, and fatigue during mechanical cycling. Each mold consists of multiple layers of laser-cut acrylic components to produce uniform rectangular beams with thickness $h \in [1.5, 3.0]$ mm, length $L = 80$ mm, and width $b = 8$ mm. The extremities of the beams are cast to blocks with a larger width (b by h by $l = 15$ by 12 by 15 mm) to emulate clamped boundary conditions.

Placement

Each beam is aligned such that its width points out of the rotary plane and is placed in a laser-cut acrylic holder that can set the compressive

strain in the range $\varepsilon \in [0.01, 0.1]$ with a resolution of ± 0.001 . These holders are mounted on a rigid disk in a way that the tilt angle can be varied in the range $\theta \in [-15^\circ, 15^\circ]$ with a resolution of $\pm 0.5^\circ$. Last, the holders are enclosed by a transparent acrylic plate to minimize air drag during rotation (see Fig. 1 and movie S1).

System parameters

In Table 1, we present the geometric parameters of the mbits used in the two experimental systems (I and II) investigated below.

Rotational apparatus

The rigid disk holding all beams is mounted to a torque motor (ETEL RTMBi140-050A) capable of delivering up to 122 Nm of peak torque. The motor is driven by a Modular AccurET 600 V/40A controller, which we program with a time series of angular positions to generate the desired velocity profile $\Omega(t)$. This setup enables precise trajectory execution, with maximum angular velocity and acceleration of $\pm 85 \text{ rad} \cdot \text{s}^{-1}$ and $\pm 10^3 \text{ rad} \cdot \text{s}^{-2}$, respectively. An encoder records the disk's angular position at 20 kHz, with an uncertainty of $\pm 8 \cdot 10^{-4}$ rad. To determine the angular velocity $\dot{\Omega}(t)$ and acceleration $\ddot{\Omega}(t)$, we apply a third-order Savitzky-Golay filter (15-point window) to the position data and perform numerical differentiation using fourth-order central finite differences.

Image analysis

The real-space configuration of each beam is imaged using a global shutter camera (IDS U3-3040SE-M-GL, with lens Vision-Lens 3.5 mm EFL, F/1.4) and is placed in the laboratory frame, above the rotating disk and aligned with its center of rotation. The shutter time is set to 100 μs to minimize image blur during rotation. We set a region of interest of 346 by 346 pixels, with 1.2 mm/pixel, to image the entire disk, setting a frame rate of 743 fps.

To quantify the configuration and dynamics of the beams, we developed an in-house image analysis algorithm with support from the EPFL Imaging Hub (F. Aymanns). First, we locate two white markers, one at the center of rotation and the other at $R = 50 \text{ mm}$ from the center of rotation (see fig. S1). Next, for every frame and all measured beams, the image analysis involves several key steps (see fig. S1 B): (i) We detect the two white markers to establish the angular position, φ , of the disk and find that it is in good agreement with the output of the encoder. (ii) A neural network, trained by manually labeling clamp corners, identifies the corners of each clamp. (iii) To approximate the neutral line of each beam, we use Hermite exponential splines from the Python library `splinesbox` (44). (iv) We strategically place five spline knots: two at the identified beam edges and three additional knots equally distributed along the beam's longitudinal axis.

(v) To precisely locate these central knots, we define three equally spaced lines normal to the clamp-to-clamp line. (vi) Last, on each line, we identify the point of maximum brightness by fitting a Gaussian function to the brightness distribution along the line. We locate the knots at the maximum of the fitted Gaussian. This image processing method achieves subpixel resolution (with $\pm 0.2 \text{ mm}$ uncertainty) in the midpoint deflection of the centerline δ and generates a time series of the centerline of each beam represented in splines (see fig. S1 c).

Definition of snap-through events

To identify the snap-through of each beam, we start from the detected midpoint deflection $\delta(t)$ and follow a four-step approach: (i) We identify the times at which the midpoint of beam i crosses its longitudinal axis $\delta_i(t_i^0) = 0$ (orange crosses, fig. S2 A, B). (ii) We define the temporal window W_i centered about t_i^0 , $W_i = [t_i^0 - 25 \text{ ms}, t_i^0 + 25 \text{ ms}]$, and determine the maximum absolute velocity $|\dot{\delta}_i|_{\text{max}}$ achieved within W_i (shaded area, fig. S2 A). (iii) We characterize the time of switching-onset t_i^* as $|\dot{\delta}_i(t_i^*)| = 0.15 |\dot{\delta}_i|_{\text{max}}$ (purple triangles, fig. S2 A). The threshold value of 0.15 was empirically optimized to provide reliable switching-onset detection across our experiments. (iv) We specify $[\Omega(t_i^*), \dot{\Omega}(t_i^*)]$ as the switching-onset in the $(\Omega, \dot{\Omega})$ -plane. We take $[\Omega(t_i^*) - \Omega(t_i^0), \dot{\Omega}(t_i^*) - \dot{\Omega}(t_i^0)]$ as an estimate of the uncertainty of the switching onsets and indicate these with faint lines.

Switching curves

We experimentally map the switching curves of each mbit by applying a set of harmonic driving protocols $\Omega(t) = a_j \sin(2\pi f_j t + \phi)$, where we fix the frequency at $f = 1.5 \text{ Hz}$, and systematically vary the amplitude $a_j \in [5.0, 80.0] \text{ rad/s}$ with steps of 5.0 rad/s and the phase $\phi = \{0, \pi\} \text{ rad}$ (see fig. S2 B, C). Before each driving protocol, we set all mbits to $s_i = 0$ for $\phi = 0$ and to $s_i = 1$ for $\phi = \pi$. This collection of driving protocols enables a precise characterization of the transition curves within the $\Omega/\dot{\Omega} < 0$ domain. To complete the transition curves across the full domain, the experimental data are mirrored about $\Omega = 0$; this symmetry operation is justified since the centrifugal force $f_\Omega \sim \Omega^2$ is independent of the sign of the velocity. As a guide to the eye for the switching-curves data in Fig. 2A, we fit a quadratic polynomial function to the measured snap-through points. To ensure a mirror symmetry about $\Omega = 0$, we consider a function without odd terms: $p(\Omega) = c_0 + c_2 \Omega^2$ (dashed and dot-dashed curves in Fig. 2A and fig. S2 C). We note that although the fitted curves give a good estimation of the location of the switching curves, selected orbits near these curves may trigger switching. Nevertheless, the selected orbits presented in this paper were repeated

Table 1. Parameters of the mbits in systems I and II. The length L , in-plane thickness h , and out-of-plane width b have an experimental uncertainty of $\pm 0.1 \text{ mm}$. The radial position R of the beams has an uncertainty of $\pm 1 \text{ mm}$. The uncertainties in compression ε and angle θ are, respectively, ± 0.001 and $\pm 0.5^\circ$.

mbit	System I		System II				
	1	2	1	2	3	4	5
L (mm)	80	80	80	80	80	80	80
h (mm)	1.9	1.9	1.6	1.9	2.1	2.3	2.6
b (mm)	8.0	8.0	8.0	8.0	8.0	8.0	8.0
R (mm)	150	150	150	150	150	150	150
ε (–)	0.050	0.015	0.015	0.026	0.037	0.055	0.060
θ ($^\circ$)	–4.5	4.5	4.5	1.5	0.0	4.5	7.5

five times and consistently demonstrated the reported switching behavior. A comprehensive characterization of the switching-curves is available in (45).

Reduced-order model

Computational spring model

In parallel with the experiments, we use a reduced-order model to guide the rational design of the mbits switching curves. This model has a configuration analogous to a von Mises truss (29–31), comprising a central point (mass m , position \mathbf{r}) connected via two linear springs (spring constant k , rest length l_0) with end points \mathbf{r}_{s1} and \mathbf{r}_{s2} (Fig. 3B). We take $\mathbf{r}_{s1} = (1 - \varepsilon)[\sin(\theta), \cos(\theta)]$, and $\mathbf{r}_{s2} = -\mathbf{r}_{s1}$, to ensure bistability for $\varepsilon > 0$. Similar to experiments, the tilt angle θ and compressive strain ε are the key design parameters. A total of four forces act on the central mass: First, the two springs give rise to the two forces $\mathbf{F}_{si} = k(\|\Delta\mathbf{r}_{si}\| - l_0)\Delta\mathbf{r}_{si} / \|\Delta\mathbf{r}_{si}\|$, where $\Delta\mathbf{r}_{si} = \mathbf{r} - \mathbf{r}_{si}$. Second, rotation gives rise to the centrifugal force $\mathbf{F}_\Omega = -m \Omega \times [\Omega \times (\mathbf{r} + R\mathbf{e}_y)]$ and Euler force $\mathbf{F}_E = -m \dot{\Omega} \times (\mathbf{r} + R\mathbf{e}_y)$, where R is the distance between the center of rotation and the position of the point mass \mathbf{r} at rest, when $(\Omega, \dot{\Omega}) = (0, 0)$. We determine the equilibrium position(s) of the mass for a given angular velocity Ω and acceleration $\dot{\Omega}$ by numerically solving the force balance using gradient descent. To find the transition curve of the reduced-order model, we determine the monostable and bistable regions of each truss.

Orbit selection

Realizing selected orbits

A target orbit can be described as $[\Omega(\tau), \dot{\Omega}(\tau)]$, where τ is a pseudo-time. Such an orbit can be realized if and only if one can find a mapping between physical time t and τ , such that

$$\dot{\Omega}(\tau) = d\Omega(\tau)/d\tau = [d\Omega(\tau)/dt] \cdot (dt/d\tau) \quad (1)$$

Since τ is a monotonically increasing function of the physical time t , this equation implies the directionality constraint on each orbit, i.e., $d\Omega(\tau)/d\tau$ has the same sign as $\dot{\Omega}(\tau)$. To construct a specific orbit, we start from a given discrete sequence of points in the $(\Omega, \dot{\Omega})$ -plane, i.e., $[\Omega(\tau), \dot{\Omega}(\tau)]$, and define τ as the trajectory index $\tau = (0, 1, 2, \dots) \cdot \Delta\tau$. We then use Eq. 1 to find $\Delta t(\tau)$

$$\Delta t(\tau) = \frac{\Omega(\tau + \Delta\tau) - \Omega(\tau)}{\dot{\Omega}(\tau)} \quad (2)$$

and map the trajectory index τ to real time as $t(\tau) = \sum_0^\tau \Delta t(\tau)$. This procedure yields a time-parametrized angular velocity profile $\Omega(t)$ that matches the selected orbit in $[\Omega(\tau), \dot{\Omega}(\tau)]$ -space and can be used as input for angular velocity-controlled experiments.

Supplementary Materials

The PDF file includes:

Figs. S1 to S4

Legends for movies S1 to S4

Other Supplementary Material for this manuscript includes the following:

Movies S1 to S4

REFERENCES

- H. Bense, M. van Hecke, Complex pathways and memory in compressed corrugated sheets. *Proc. Natl. Acad. Sci. U.S.A.* **118**, e2111436118 (2021).
- W. Liu, S. Janbaz, D. Dykstra, B. Ennis, C. Coulais, Harnessing plasticity in sequential metamaterials for ideal shock absorption. *Nature* **634**, 842–847 (2024).
- L. J. Kwakernaak, M. van Hecke, Counting and sequential information processing in mechanical metamaterials. *Phys. Rev. Lett.* **130**, 268204 (2023).
- M. Mungan, S. Sastry, K. Dahmen, I. Regev, Networks and hierarchies: How amorphous materials learn to remember. *Phys. Rev. Lett.* **123**, 178002 (2019).
- M. van Hecke, Profusion of transition pathways for interacting hysterons. *Phys. Rev. E* **104**, 054608 (2021).
- N. C. Keim, J. D. Paulsen, Multiperiodic orbits from interacting soft spots in cyclically sheared amorphous solids. *Sci. Adv.* **7**, eabg7685 (2021).
- C. W. Lindeman, S. R. Nagel, Multiple memory formation in glassy landscapes. *Sci. Adv.* **7**, eabg7133 (2021).
- J. Ding, M. van Hecke, Sequential snapping and pathways in a mechanical metamaterial. *J. Chem. Phys.* **156**, 204902 (2022).
- D. Shohat, D. Hexner, Y. Lahini, Memory from coupled instabilities in unfolded crumpled sheets. *Proc. Natl. Acad. Sci. U.S.A.* **119**, e2200028119 (2022).
- D. Melancon, A. E. Forte, L. M. Kamp, B. Gorissen, K. Bertoldi, Inflatible origami: Multimodal deformation via multistability. *Adv. Funct. Mater.* **32**, 2201891 (2022).
- T. Jules, A. Reid, K. E. Daniels, M. Mungan, F. Lechenault, Delicate memory structure of origami switches. *Phys. Rev. Res.* **4**, 013128 (2022).
- C. W. Lindeman, T. R. Jalowiec, N. C. Keim, Generalizing multiple memories from a single drive: The hysteron latch. *Sci. Adv.* **11**, eadr5933 (2025).
- J. L. Silverberg, A. A. Evans, L. McLeod, R. C. Hayward, T. Hull, C. D. Santangelo, I. Cohen, Using origami design principles to fold reprogrammable mechanical metamaterials. *Science* **345**, 647–650 (2014).
- T. Chen, M. Pauly, P. M. Reis, A reprogrammable mechanical metamaterial with stable memory. *Nature* **589**, 386–390 (2021).
- M. Mirzajanzadeh, D. Pasini, Reprogrammable curved-straight origami: Multimorphability and volumetric tunability. *Sci. Adv.* **11**, eadu4678 (2025).
- E. T. Filipov, T. Tachi, G. H. Paulino, Origami tubes assembled into stiff, yet reconfigurable structures and metamaterials. *Proc. Natl. Acad. Sci. U.S.A.* **112**, 12321–12326 (2015).
- R. Guseinov, C. McMahan, J. Pérez, C. Daraio, B. Bickel, Programming temporal morphing of self-actuated shells. *Nat. Commun.* **11**, 237 (2020).
- A. S. Meeussen, M. van Hecke, Multistable sheets with rewritable patterns for switchable shape-morphing. *Nature* **621**, 516–520 (2023).
- M. A. McEvoy, N. Correll, Materials that couple sensing, actuation, computation, and communication. *Science* **347**, 1261689 (2015).
- C. Kaspar, B. J. Ravoo, W. G. van der Wiel, S. V. Wegner, W. H. P. Pernice, The rise of intelligent matter. *Nature* **594**, 345–355 (2021).
- H. Yasuda, P. R. Buskohl, A. Gillman, T. D. Murphey, S. Stepney, R. A. Vaia, J. R. Raney, Mechanical computing. *Nature* **598**, 39–48 (2021).
- C. El Helou, B. Grossmann, C. E. Tabor, P. R. Buskohl, R. L. Harne, Mechanical integrated circuit materials. *Nature* **608**, 699–703 (2022).
- C. Sirote-Katz, D. Shohat, C. Merrigan, Y. Lahini, C. Nisoli, Y. Shokef, Emergent disorder and mechanical memory in periodic metamaterials. *Nat. Commun.* **15**, 4008 (2024).
- C. M. Meulblok, A. Singh, M. Labousse, M. van Hecke, Path-dependency and emergent computing under vectorial driving. arXiv:2503.07764 [cond-mat.soft] (2025).
- M. M. Terzi, M. Mungan, State transition graph of the preisach model and the role of return-point memory. *Phys. Rev. E* **102**, 012122 (2020).
- A. Guerra, A. C. Slim, D. P. Holmes, O. Kodio, Self-ordering of buckling, bending, and bumping beams. *Phys. Rev. Lett.* **130**, 148201 (2023).
- C. M. Meulblok, M. van Hecke, Transients and multiperiodic responses: A hierarchy of material bits. arXiv:2505.09517 [cond-mat.soft] (2025).
- E. Gutierrez-Prieto, M. Gomez, P. M. Reis, Harnessing centrifugal and Euler forces for tunable buckling of a rotating elastica. *Extreme Mech. Lett.* **72**, 102246 (2024).
- R. V. Mises, Über die stabilitätsprobleme der elastizitätstheorie. *Zamm-zeitschrift Fur Angewandte Mathematik Und Mechanik* **3**, 406–422 (1923).
- P. X. Bellini, The concept of snap-buckling illustrated by a simple model. *Int. J. Non-Linear Mech.* **7**, 643–650 (1972).
- Z. Bazant, L. Cedolin, *Stability of Structures: Elastic, Inelastic, Fracture and Damage Theories* (World Scientific, 2010).
- D. M. J. Dykstra, J. Busink, B. Ennis, C. Coulais, Viscoelastic snapping metamaterials. *J. Appl. Mech.* **86**, 111012 (2019).
- D. M. J. Dykstra, S. Janbaz, C. Coulais, The extreme mechanics of viscoelastic metamaterials. *APL Mater.* **10**, 080702 (2022).
- T. Jules, L. Michel, A. Douin, F. Lechenault, When the dynamical writing of coupled memories with reinforcement learning meets physical bounds. *Commun. Phys.* **6**, 25 (2023).
- C. W. Lindeman, V. F. Hagh, C. I. Ip, S. R. Nagel, Competition between energy and dynamics in memory formation. *Phys. Rev. Lett.* **130**, 197201 (2023).
- L. Jin, M. van Hecke, Dynamic avalanches: Rate-controlled switching and race conditions. arXiv:2507.02387 [cond-mat.soft] (2025).
- J. B. Geddes, B. D. Storey, D. Gardner, R. T. Carr, Bistability in a simple fluid network due to viscosity contrast. *Phys. Rev. E* **81**, 046316 (2010).

38. A. Martínez-Calvo, M. D. Biviano, A. H. Christensen, E. Katifori, K. H. Jensen, M. Ruiz-García, The fluidic memristor as a collective phenomenon in elasto-hydrodynamic networks. *Nat. Commun.* **15**, 3121 (2024).
39. B. van Sluijs, R. J. M. Maas, A. J. van der Linden, T. F. A. de Greef, W. T. S. Huck, A microfluidic optimal experimental design platform for forward design of cell-free genetic networks. *Nat. Commun.* **13**, 3626 (2022).
40. L. E. Altman, N. Aguilar, D. J. Durian, M. Ruiz-García, E. Katifori, Collective behavior and memory states in flow networks with tunable bistability. arXiv:2502.05570 [cond-mat.soft] (2025).
41. M. Gomez, D. E. Moulton, D. Vella, Passive control of viscous flow via elastic snap-through. *Phys. Rev. Lett.* **119**, 144502 (2017).
42. P. Grandgeorge, T. G. Sano, P. M. Reis, An elastic rod in frictional contact with a rigid cylinder. *J. Mech. Phys. Solids* **164**, 104885 (2022).
43. P. Leroy-Calatayud, M. Pezzulla, A. Keiser, K. Mulleners, P. M. Reis, Tapered foils favor traveling-wave kinematics to enhance the performance of flapping propulsion. *Phys. Rev. Fluids* **7**, 074403 (2022).
44. F. Aymanns, E. Andó, V. Uhlmann, SplineBox, 2024. Version 0.2.0; <https://pypi.org/project/splinebox/>.
45. E. Gutierrez-Prieto, G. Yakir, P. M. Reis, High-throughput characterization of snap-through stability boundaries of bistable beams in a programmable rotating platform. arXiv:2512.09544 [cond-mat.soft] (2025).
46. ISO IEC 8859-1:1998, 8-bit single-byte coded graphic character sets—Part 1: Latin alphabet no. 1 (International Organization for Standardization, 1998).

Acknowledgments: We acknowledge the EPFL Center for Imaging, especially F. Aymanns, for assistance/help with developing the image processing pipeline. **Funding:** C.M.M. and M.v.H. acknowledge funding from European Research Council Grant ERC-101019474.

Author contributions: P.M.R.: Writing—original draft, conceptualization, writing—review and editing, methodology, supervision, project administration, and visualization. E.G.-P.: Writing—original draft, conceptualization, investigation, writing—review and editing, methodology, resources, data curation, validation, formal analysis, software, and visualization. C.M.M.: Writing—original draft, conceptualization, investigation, writing—review and editing, methodology, validation, formal analysis, software, and visualization. M.v.H.: Writing—original draft, conceptualization, writing—review and editing, resources, funding acquisition, supervision, project administration, and visualization. **Competing interests:** The authors declare that they have no competing interests. **Data, code, and materials availability:** All data and code needed to evaluate and reproduce the results in the paper are present in the paper, the Supplementary Materials, and the Zenodo repository <https://doi.org/10.5281/zenodo.18703706>. Correspondence and requests for materials should be addressed to P.M.R. (pedro.reis@epfl.ch) and M.v.H. (M.v.Hecke@amolf.nl or mvhecke@physics.leidenuniv.nl).

Submitted 9 September 2025

Accepted 2 April 2026

Published 6 May 2026

10.1126/sciadv.aec1606

Dynamic drives allow independent control of material bits for targeted memory

Eduardo Gutierrez-Prieto, Colin M. Meulblok, Martin van Hecke, and Pedro M. Reis

Sci. Adv. **12** (19), eaec1606. DOI: 10.1126/sciadv.aec1606

View the article online

<https://www.science.org/doi/10.1126/sciadv.aec1606>

Permissions

<https://www.science.org/help/reprints-and-permissions>

Use of this article is subject to the [Terms of service](#)

Science Advances (ISSN 2375-2548) is published by the American Association for the Advancement of Science, 1200 New York Avenue NW, Washington, DC 20005. The title *Science Advances* is a registered trademark of AAAS.

Copyright © 2026 The Authors, some rights reserved; exclusive licensee American Association for the Advancement of Science. No claim to original U.S. Government Works. Distributed under a Creative Commons Attribution NonCommercial License 4.0 (CC BY-NC).